electronic reprint

STRUCTURAL BIOLOGY
COMMUNICATIONS

ISSN: 2053-230X
journals.iucr.org/f

Structural analysis of the tetrahydrobiopterin glucosyltransferase *Ps*BGluT from *Pseudanabaena* sp. Chao 1811

Ruijie Zang, Yongliang Jiang and Cong-Zhao Zhou

Acta Cryst. (2025). F**81**, 495–504

STRUCTURAL BIOLOGY COMMUNICATIONS

ISSN 2053-230X

Structural analysis of the tetrahydrobiopterin glucosyltransferase *Ps*BGluT from *Pseudanabaena* sp. Chao 1811

Ruijie Zang,[a] Yongliang Jiang[b]* and Cong-Zhao Zhou[b]*

[a]Division of Life Sciences and Medicine, University of Science and Technology of China, Huang Shan Road, Hefei, Anhui 230026, People's Republic of China, and [b]University of Science and Technology of China, Huang Shan Road, Hefei, Anhui 230026, People's Republic of China. *Correspondence e-mail: jyl@mail.ustc.edu.cn, zcz@ustc.edu.cn

Received 16 June 2025
Accepted 27 October 2025

Edited by M. J. Romao, Universidade Nova de Lisboa, Portugal

Keywords: tetrahydrobiopterin; GT-B glycosyltransferases; crystallography; *Ps*BGluT.

PDB references: apo *Ps*BGluT, 9v0w; *Ps*BGluT–UDP, 9v0l

Supporting information: this article has supporting information at journals.iucr.org/f

Pterin glycosides are widely distributed in cyanobacteria and have been implicated in the regulation of phototaxis and photosynthesis. Here, we identified a new uridine diphosphate glucose:tetrahydrobiopterin α-glucosyltransferase, termed *Ps*BGluT, from *Pseudanabaena* sp. Chao 1811, which catalyzes the formation of pterin glycosides. We solved crystal structures of apo *Ps*BGluT and its UDP-bound form at 2.8 and 2.3 Å resolution, respectively. *Ps*BGluT forms a homodimer, with each subunit adopting a canonical GT-B fold composed of two Rossmann-like domains. Structural analysis combined with molecular docking revealed the binding sites for both the donor UDP-glucose and the acceptor tetrahydrobiopterin. Based on these findings, we proposed that *Ps*BGluT operates via an S_Ni retaining catalytic mechanism. This study advances our understanding of pteridine glycosylation and also provides a structural basis for investigating the photosynthetic signaling pathways in cyanobacteria.

1. Introduction

Pterins are widely distributed in nature and commonly function as coenzymes in the biosynthesis of various metabolites, including aromatic amino acids, nitric oxide, neurotransmitters and nucleic acids (Iyer *et al.*, 2021). They are essential for the normal growth and metabolic homeostasis of diverse organisms. For example, microorganisms deficient in tetrahydromonapterin synthesis exhibit impaired growth on media lacking tyrosine, as tyrosine biosynthesis by phenylalanine hydroxylase depends on tetrahydromonapterin as a coenzyme (Li *et al.*, 2025). Similarly, human infants with tetrahydrobiopterin (BH_4) synthesis deficiencies develop hyperphenylalaninemia, a condition that can cause severe neurological damage (Shyam *et al.*, 2024).

Ultraviolet light can penetrate the ozone layer and poses a threat to photoautotrophs by generating reactive oxygen species (ROS) that damage the photosynthetic machinery (Singh *et al.*, 2023). Pterin glycosides, which have strong absorbance in the UV spectrum, help to protect photosynthetic pigments from UV-induced damage (Noguchi *et al.*, 1999). Pterin glycosides, which are synthesized from pterins by glycosyltransferases (GTs; Choi *et al.*, 2001), play important roles in cyanobacteria, such as regulating phototaxis (Singh *et al.*, 2023) and normal cell growth (Choi *et al.*, 2001).

Glycosyltransferases catalyze the transfer of glycosyl groups from sugar donors to sugar acceptors. They are generally classified into three major folds according to their structures: GT-A and GT-B, both of which harbor two Rossmann-like folds, and GT-C, which is a membrane-protein type

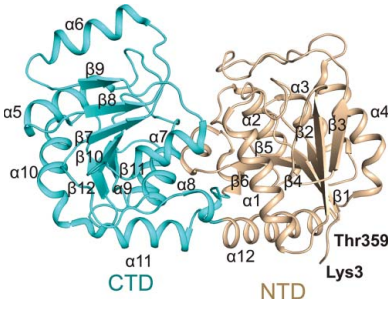

(Alexander & Locher, 2023; Lairson *et al.*, 2008; Khaled *et al.*, 2025). On the basis of their catalytic mechanisms, glycosyltransferases can be grouped into inverting GTs that invert the configuration during the catalytic reaction and retaining GTs that preserve the configuration of the glycosidic bond in the product (Guerin, 2023).

In a previous study, we isolated a new cyanobacterial strain, *Pseudanabaena* sp. Chao 1811, from the Nanfei estuary of Lake Chaohu, China (Zhu *et al.*, 2023). Genomic analysis of *Pseudanabaena* sp. Chao 1811 identified a hypothetical UDP-glucose:tetrahydrobiopterin α-glucosyltransferase (termed *Ps*BGluT; NCBI accession WP_271251925.1). Here, we solved crystal structures of apo *Ps*BGluT and its UDP-bound form, which reveal a classical GT-B glycosyltransferase possessing two distinct $\beta/\alpha/\beta$ Rossmann-like fold domains. Structural analyses, together with biochemical and enzymatic activity assays, enabled us to identify the active-site pocket responsible for binding to the donor UDP-glucose (UDP-Glc) and the acceptor tetrahydrobiopterin (BH_4). These findings increase the understanding of pteridine glycosylation and provide insights into the strategies employed by photoautotrophs to maintain efficient photosynthesis.

2. Materials and methods

2.1. Macromolecule production

The *Ps*BGluT gene was inserted into the pET-28a vector with an N-terminal 6×His tag. The cells were cultured at 37°C in 1 l LB medium containing 30 µg ml^{-1} kanamycin to an OD_{600} of between 0.5 and 0.8. *Ps*BGluT overexpression was initiated by the addition of 0.2 m*M* isopropyl β-D-1-thiogalactopyranoside at 16°C for 20 h. Afterwards, the cells were harvested via centrifugation and resuspended in 40 ml lysis buffer (0.05 *M* NaH_2PO_4 pH 7.5). Ultrasonication was then conducted using an ultrasonic processor (VC750, SONICS, USA) with a total processing duration of 30 min. The treatment was applied in pulsed cycles consisting of 2 s sonication followed by a 2 s interval at 42% amplitude, resulting in an effective sonication time of 15 min. The supernatant was harvested by high-speed centrifugation (4°C, 30 min, 12 000*g*) and was then transferred onto an Ni–NTA column (GE Healthcare) containing 4 ml Ni–NTA resin pre-equilibrated with lysis buffer. The target protein at 12–18 mg ml^{-1} was eluted with 6 ml buffer supplemented with 0.5 *M* imidazole. The target protein then underwent gel-filtration chromatography on a Superdex 75 pg HiLoad 16/600 column (Cytiva). For crystallization of the *Ps*BGluT–UDP complex and enzymatic assays, the protein was purified by gel-filtration chromatography in 0.05 *M* NaH_2PO_4 pH 7.5. For crystallization of apo *Ps*BGluT, gel-filtration chromatography was performed with 0.05 *M* NaH_2PO_4 pH 6.5 (Table 1).

2.2. Crystallization of *Ps*BGluT

After concentration to 0.5 m*M* (20 mg ml^{-1}) in 0.05 *M* NaH_2PO_4 pH 6.5, apo *Ps*BGluT was crystallized via sitting-drop vapor diffusion by mixing 1 µl protein solution with 1 µl precipitant solution (1.0 *M* ammonium sulfate, 0.1 *M* Tris pH 8.0) at 285 K.

Table 1
Macromolecule-production information.

Protein	*Ps*BGluT
Source organism	*Pseudanabaena* sp. Chao 1811
DNA source (1092 bp)	Polymerase chain reaction
Forward primer	TCATCATCACAGCAGCGGCATGAATAAA AAATATCGGTTAC
Reverse primer	AGTCATGCTAGCCATATGCTAGATATTT CTAGATAGGG
Expression vector	pET-28a
Expression host	*Escherichia coli* C43 (DE3)
Complete amino-acid sequence of the construct produced (377 amino acids)	MGSSHHHHHHSSGMNKKYRLLFLSTPVG ALGSGIGGGVELTLQNAAKALMAKGHE VEIVAPEGSVTNVTKLTPIAGNSQVSA QTQVGTDMVVLPQDSVLENMWSYAREV QDQFDLLFNFAYDWLPLYLTPFFHRPI AHWISMSSLSPVIDAMVSKTVKLCPQA IAVNTRACADTFSDGDRLMIMGKGIDV TQYNFVAKPEKPSLAWVGRISPEKGLE DAAETAQATGLPLRVFGLIQDQAYWQQ IQNDFPKAEIHYEGFLSTHELQQKLGQ SSALLMTPRWIEAFGNAAIEAFACGVP VISYRSGGLTEIVRHGKTGFLVDMGSV AGLIEAVSKLETIDRLACRQQLEEEYS LEVWGDRLEKWFEQLITSYTLSRNI

For the *Ps*BGluT–UDP complex, 0.5 m*M* *Ps*BGluT was mixed with 5 m*M* Na_2UDP-Glc (Macklin, China) in 0.05 *M* NaH_2PO_4 pH 7.5. The mixture was placed on ice for 30 min. Crystals were obtained via sitting-drop vapor diffusion within four days by mixing 1 µl protein solution with 1 µl precipitant solution (0.1 *M* sodium acetate pH 5.0, 2.0 *M* sodium formate) at 285 K (Table 2).

2.3. Data collection and processing

We collected X-ray diffraction data for apo *Ps*BGluT at 100 K using Cu X-rays generated by a MicroMax-007 HF rotating-anode X-ray generator (Rigaku, Japan) equipped with a PILATUS 200K detector. The data were indexed and integrated with *CrysAlis^{Pro}* (Agilent Technologies, Yarnton, England) and scaled using *AIMLESS* (Evans & Murshudov, 2013) from the *CCP*4 suite (Agirre *et al.*, 2023). The *Ps*BGluT–UDP data were collected in the same way (Table 3).

2.4. Structure solution and refinement

The apo *Ps*BGluT structure was determined via molecular replacement (MR) in *MOLREP* (Vagin & Teplyakov, 2010) using an *AlphaFold*2 (Jumper *et al.*, 2021) predicted structure as a search model. The initial model of *Ps*BGluT was rebuilt and refined by *Phenix* (Poon *et al.*, 2024) with NCS restraints and TLS, and was manually adjusted with *WinCoot* (Casañal *et al.*, 2020). All structural figures were prepared using *PyMOL* (Schrödinger).

The crystal structure of the *Ps*BGluT–UDP complex was solved by MR using the apo *Ps*BGluT structure as the search model. Chain *B* of the apo *Ps*BGluT structure was divided into two domains, comprising residues Met3–Ile170 and Met171–Ile360, which were independently used as search models in *MOLREP*. The resulting model was automatically refined

Table 2
Crystallization conditions for apo *Ps*BGluT and *Ps*BGluT–UDP.

	Apo *Ps*BGluT	*Ps*BGluT–UDP
Method	Vapor diffusion, sitting drop	Vapor diffusion, sitting drop
Plate type	XtalQuest plate	XtalQuest plate
Temperature (K)	285	285
Protein concentration (mg ml^{-1})	20	20
Buffer composition of protein solution	50 m*M* NaH_2PO_4 pH 6.5	50 m*M* NaH_2PO_4 pH 7.5
Composition of reservoir solution	0.1 *M* Tris pH 8.0, 1 *M* ammonium sulfate	0.1 *M* sodium acetate pH 5.0, 2.0 *M* sodium formate
Volume and ratio of drop	2 µl, 1:1	2 µl, 1:1
Volume of reservoir (µl)	100	100

Table 3
Data collection.

Values in parentheses are for the outer shell.

	Apo *Ps*BGluT	*Ps*BGluT–UDP
Diffraction source	MicroMax-007 HF	MicroMax-007 HF
Wavelength (Å)	1.54184	1.54184
Temperature (K)	100	100
Detector	Dectris PILATUS3 R 200K-A	Dectris PILATUS3 R 200K-A
Crystal-to-detector distance (mm)	110	110
Rotation range per image (°)	0.15	0.15
Total rotation range (°)	360	360
Exposure time per image (s)	50	50
Space group	$P6_122$	$P6_122$
a, *b*, *c* (Å)	162.21, 162.21, 181.95	176.97, 176.97, 66.17
α, β, γ (°)	90, 90, 120	90, 90, 120
Mosaicity (°)	0.60	0.86
Resolution range (Å)	13.25–2.80 (2.94–2.80)	13.04–2.30 (2.39–2.30)
Total No. of reflections	525994 (52542)	380341 (28771)
No. of unique reflections	34964 (4609)	27426 (2848)
Completeness (%)	99.0 (100.0)	99.4 (100.0)
Multiplicity	15.0 (11.4)	13.9 (10.1)
$\langle I/\sigma(I)\rangle$	18.3 (2.0)	24.7 (6.3)
$R_{p.i.m.}$	0.044 (0.576)	0.029 (0.160)
Overall *B* factor from Wilson plot (Å^2)	51.329	18.6
$CC_{1/2}$	0.999 (0.793)	0.999 (0.916)

Table 4
Structure refinement.

Values in parentheses are for the outer shell.

	Apo *Ps*BGluT	*Ps*BGluT–UDP
Resolution range (Å)	13.25–2.80 (2.94–2.80)	13.04–2.30 (2.39–2.30)
Completeness (%)	99.56	99.4
No. of reflections, working set	33073 (2693)	26113 (2834)
No. of reflections, test set	1699 (143)	1293 (148)
Final R_{cryst}	0.2397 (0.3282)	0.2143 (0.3107)
Final R_{free}	0.2723 (0.3711)	0.2637 (0.3782)
No. of non-H atoms		
Protein	5548	2807
Ion	0	
Ligand	0	1
Water	92	218
Total	5640	3025
R.m.s. deviations†		
Bond lengths (Å)	0.006	0.004
Angles (°)	0.857	0.682
Average *B* factor (Å^2)	78.46	29.81
Ramachandran plot†		
Most favored (%)	98.03	97.18
Allowed (%)	1.97	2.54
Disallowed (%)	0	0.28‡
PDB code	9v0w	9v0l

† Calculated by *phenix.molprobity*. ‡ Ala195 is not in the allowed region.

with *REFMAC*5 (Kovalevskiy *et al.*, 2018). The initial model was subsequently rebuilt and refined in *Phenix*, followed by manual adjustments in *WinCoot*. Notably, the substrate UDP-Glc was probably hydrolyzed by *Ps*BGluT during crystallization, leaving only the product UDP visible in the final structure. The final structures were deposited in the PDB.

Data-reduction and refinement statistics are shown in Table 4.

2.5. Docking calculation

Molecular docking of BH_4 with *Ps*BGluT was performed via *AutoDock* 4.2.6 (Morris *et al.*, 2009). The structure of *Ps*BGluT–UDP with water molecules removed was selected as the docking model. H atoms were then added to both *Ps*BGluT–UDP and BH_4, and the torsional degrees of freedom for BH_4 were defined. The grid box parameters were set with a grid point spacing of 0.375 Å, and the grid dimensions were specified as 54 × 54 × 40 points, with the central grid point at coordinates (13.263, 59.296, 4.187). BH_4 was placed within the grid box, and genetic algorithm (GA) runs were performed to generate ten docking poses. The top-ranked pose, with a binding energy of −8.4 kcal mol^{-1}, was selected for further analysis of the docking pattern using *PyMOL*.

2.6. Isothermal titration calorimetry

We utilized a MicroCal PEAQ-ITC (Malvern Panalytical, UK) to evaluate the interactions between *Ps*BGluT and UDP-Glc or BH_4. Initially, *Ps*BGluT and Na_2UDP-Glc were dissolved in lysis buffer. 20 injections (2 µl per injection, excluding the first) of Na_2UDP-Glc (10 m*M*; Macklin, China) were titrated into *Ps*BGluT (0.5 m*M*) with an injection interval of 2 min at a temperature of 25°C. In BH_4 titration, the titrate and titrand were BH_4·2HCl (1 m*M*; Macklin, China) and *Ps*BGluT (0.1 m*M*), respectively, and the titration was executed like that for Na_2UDP-Glc. We analyzed the data using the *MicroCal PEAQ-ITC Analysis Software* (Malvern Panalytical).

2.7. Enzymatic activity assays

The reaction was performed as reported previously, with further optimization of the reaction system, to assess whether *Ps*BGluT is capable of transferring glucose to BH_4 (Choi *et al.*, 2001). The reaction system consisted of 10 µ*M* *Ps*BGluT, 0.2% L-ascorbic acid (Macklin, China), 500 µ*M* Na_2UDP-Glc

(Macklin, China), 50 µ*M* BH_4·2HCl (Macklin, China) and 0.05 *M* NaH_2PO_4 pH 7.5. The reaction was conducted for 30 min at 37°C. The BH_4 in the mixture was then oxidized to biopterin by adding 100 µl 2% NaI, 1% I_2, 1 *M* HCl and incubating in the dark for 1 h. After oxidation, 20 µl 5% L-ascorbic acid was added to the mixture to terminate the oxidation. The supernatant was harvested by centrifugation and analyzed by high-performance liquid chromatography using an Agilent 1260 Infinity II instrument (USA). Samples of 5 µl were applied onto a C18 column (4.6 × 250 mm, 5 µm, XtalBridge, Waters, USA) equilibrated with 10 m*M* KH_2PO_4: methanol [92:8(*v*:*v*)]. Isocratic elution was performed at a flow rate of 1 ml min^{-1}, monitoring the fluorescence of biopterin using an excitation wavelength of 350 nm and an emission wavelength of 450 nm (Mu *et al.*, 2022). The reaction system in the absence of *Ps*BGluT was used as a control.

2.8. Mass-photometry test

We utilized the TwoMP apparatus (Refeyn, UK) to detect *Ps*BGluT oligomers in solution. Initially, we placed microscope cover slips (Thorlabs) into the flow chamber, and silicone gaskets (Grace Bio-Labs, 3 × 2) were placed onto the cover slips to load samples properly. Mass-contrast calibration was executed via measurement of the contrast of bovine serum albumin, generating a calibration curve (R^2 = 0.999, maximum mass error = 5.5%) that was matched in the *Refeyn Discover-MP* software to compute the molecular-mass distribution of protein molecules in solution during analysis.

Before analysis, we injected 15 l fresh lysis buffer adjusted to 25°C into a well to find the focal position. Thereafter, diluted protein samples were completely mixed with the aforementioned lysis buffer. Using the regular image-acquisition mode of the *Refeyn AcquireMP* software, we ultimately obtained a 60 s movie (100 frames s^{-1}) in each test. Finally, using *Refeyn DiscoverMP*, we analyzed the data by fitting each histogram with a normal distribution to calculate the molecular mass (kDa) and counts of *Ps*BGluT molecules in solution.

3. Results and discussion

3.1. *Ps*BGluT is a uridine diphosphate glucose: tetrahydrobiopterin glucosyltransferase

Sequence analysis revealed that *Ps*BGluT has high sequence similarity to pterin glycosyltransferases (Supplementary Fig. S1; Lee *et al.*, 2010). To test whether *Ps*BGluT functions as a pterin glycosyltransferase, we expressed and purified the protein in *Escherichia coli*, yielding *Ps*BGluT protein with high homogeneity (Supplementary Fig. S2). Mass photometry revealed that *Ps*BGluT, which has a monomer molecular mass of around 40 kDa, mainly exists as a dimer in solution (Fig. 1*a*). Isothermal titration calorimetry assays revealed that *Ps*BGluT could specifically bind to BH_4 and UDP-Glc, with dissociation constants (K_d) of 69.8 ± 26.7 and 969 ± 73.4 µ*M*, respectively (Figs. 1*b* and 1*c*). Subsequent enzymatic activity assays via high-performance liquid chromatography (HPLC) revealed that *Ps*BGluT could transfer the glucose moiety from UDP-Glc to BH_4, forming the product BH_4-glucoside (Fig. 1*d*). These results clearly suggest that *Ps*BGluT is indeed a uridine diphosphate glucose:tetrahydrobiopterin glucosyltransferase.

3.2. Overall structure of dimeric *Ps*BGluT

In the crystal structure of apo *Ps*BGluT, each asymmetric unit possesses two subunits that form a stable dimer (Figs. 2*a* and 2*b*). *Ps*BGluT exhibits a typical GT-B fold (Huang *et al.*, 2024), which comprises an N-terminal domain (NTD) and a C-terminal domain (CTD). Both domains adopt a $\beta/\alpha/\beta$ Rossmann-like fold structure, with the catalytic center located in the interdomain cleft (Fig. 2*c*). The NTD (residues Lys3–Ile170 and Glu341–Leu360) features a six-stranded parallel β-sheet with order 3–2–1–4–5–6, sandwiched by five α-helices (α1–α4 and α12), in which α12 is aligned perpendicular to α1–α4 (Fig. 2*c*). The CTD (residues Met171–Leu340) contains a six-stranded parallel β-sheet with order 9–8–7–10–11–12, wrapped by six α-helices (α5–α10) on both sides (Fig. 2*c*). Notably, the NTD of *Ps*BGluT features a unique long loop (residues Ala62–Ser84, termed L1) connecting β3 and α2, which is much longer than those in other GT-B glycosyltransferases (Supplementary Fig. S3). The L1 loop, which is located near the catalytic crevice, is rich in hydrophobic residues (Supplementary Figs. S1 and S3*a*) and might play a role in accommodating the acceptor pterin harboring a hydrophobic ring.

The two *Ps*BGluT subunits form a stable dimer with an interior interface area of approximately 1050 Å^2 (Fig. 2*a*). The NTDs of the two subunits mediate dimer formation via widespread hydrophobic interactions. Of note, helices α2, α3 and α4, as well as loop 76–84, of one monomer and their counterparts in the other monomer are arranged in a rotational symmetry that stabilizes the dimer interface (Fig. 2*b*). Moreover, four salt bridges (Asp83–Lys142′, Asp87–Lys142′ and vice versa) further enhance the stability of the dimeric interface (Fig. 2*b*). The residues involved in the dimeric interface are highly conserved among pterin glycosyltransferases (Supplementary Fig. S1), suggesting that dimerization of these pterin glycosyltransferases might be required for the proper assembly and biological functions.

3.3. Alignment of *Ps*BGluT with other glycosyltransferases

A structural homolog search via the *DALI* server (Holm *et al.*, 2023) showed that the *Ps*BGluT structure is similar to that of the UDP-Glc:BH_4 glucosyltransferase BGluT from *Synechococcus* sp. PCC 7942 (PDB entry 5ze7, apo form; Fig. 2*d*), with an r.m.s.d. of 2.286 Å over 338 C^α atoms (Choi *et al.*, 2001). Nonetheless, drastic structural differences exist between *Ps*BGluT and BGluT (Figs. 2*d* and 2*e*). Firstly, the inter-domain crevice between the NTD and CTD is smaller in *Ps*BGluT compared with BGluT (Fig. 2*d*), and on superimposing the NTDs in the *Ps*BGluT and BGluT structures we observed a 12° rotation between the two CTDs (Fig. 2*e*).

Secondly, the two α-helices at the C-terminus of *Ps*BGluT are replaced by a single long α-helix in BGluT (Fig. 2*d*).

In addition, the oligomerization states and the dimeric interface of *Ps*BGluT differ from those of its homologs. In *Ps*BGluT, the three α-helices at the dimeric interface are arranged parallel to their counterparts (Fig. 2*b*). In contrast, the three corresponding α-helices at the dimeric interface in Alr3699 from *Anabaena* sp. PCC 7120 (PDB entry 4xso; Wang *et al.*, 2016) are arranged perpendicular to their counterparts (Supplementary Fig. S4*a*). Moreover, compared with Alr3699, *Ps*BGluT contains an additional loop, Asp72–Ser84, that further stabilizes the dimeric interface. Additionally, the dimeric structure of *Ps*BGluT differs from that of the tetrameric AtSUS from *Arabidopsis thaliana* (PDB entry 3s27, Supplementary Figs. S4*b* and S4*c*), which possesses two distinct stable dimeric interfaces (Zheng *et al.*, 2011), or the monomeric SenB from *Variovorax paradoxus*, which lacks interfaces (Huang *et al.*, 2024).

3.4. The active-site pocket of *Ps*BGluT

In the *Ps*BGluT–UDP complex structure, a molecule of UDP specifically binds to the CTD (Figs. 3*a* and 3*b*; Supplementary Fig. S5). Compared with apo *Ps*BGluT, UDP binding induces a conformational change in *Ps*BGluT, bringing the CTD and NTD closer to each other. On superimposing the

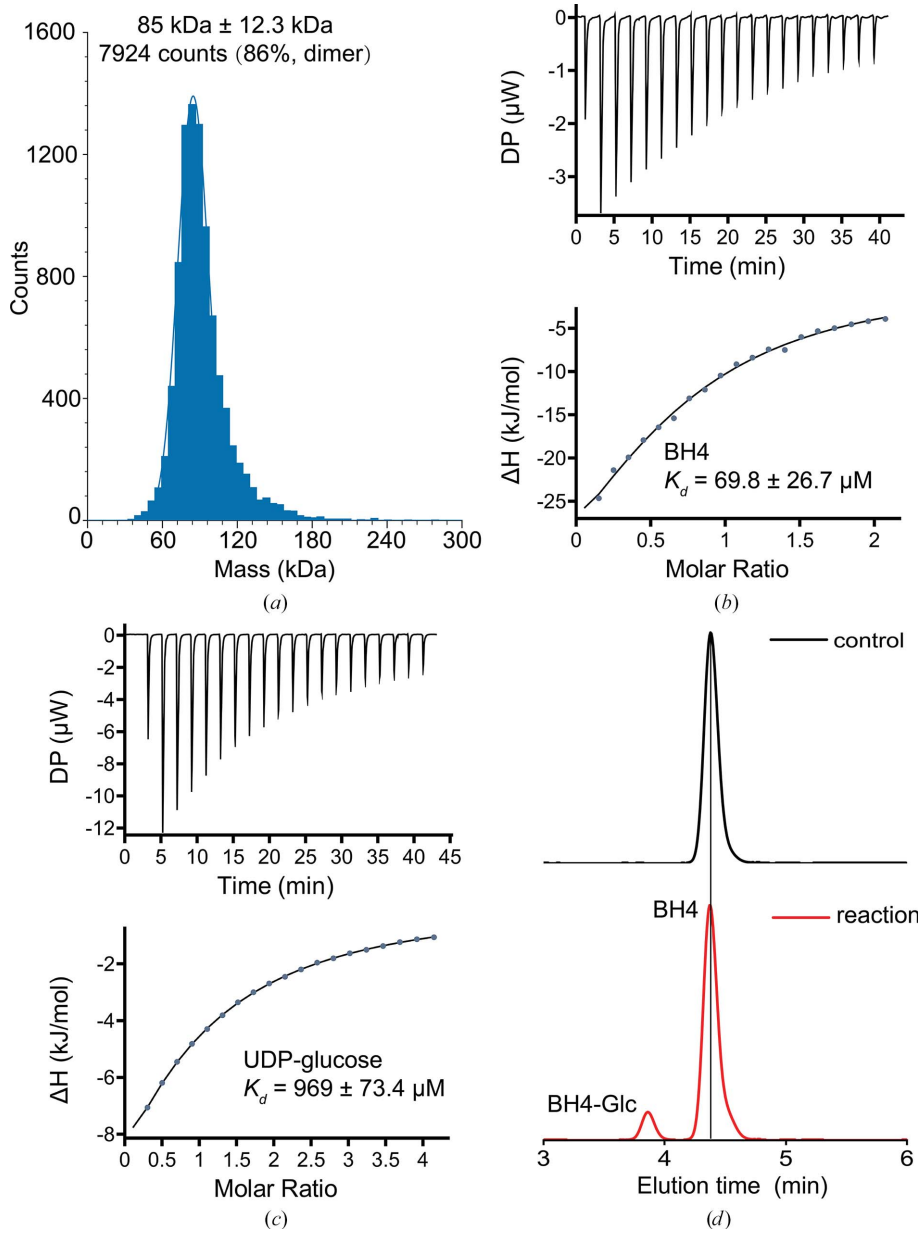

Figure 1
Biochemical characterization of *Ps*BGluT. (*a*) Mass photometry of *Ps*BGluT at 50 n*M*. The molecular mass corresponding to the protein peak is labeled. (*b*, *c*) ITC curves showing the affinity of *Ps*BGluT for tetrahydrobiopterin (BH_4) or UDP-glucose (UDP-Glc). The dissociation constants (K_d) between *Ps*BGluT and the substrates are labeled. (*d*) HPLC analysis of tetrahydrobiopterin glucosylation catalyzed by *Ps*BGluT. The peaks for BH_4 and the product tetrahydrobiopterin glucoside (BH_4-Glc) are labeled.

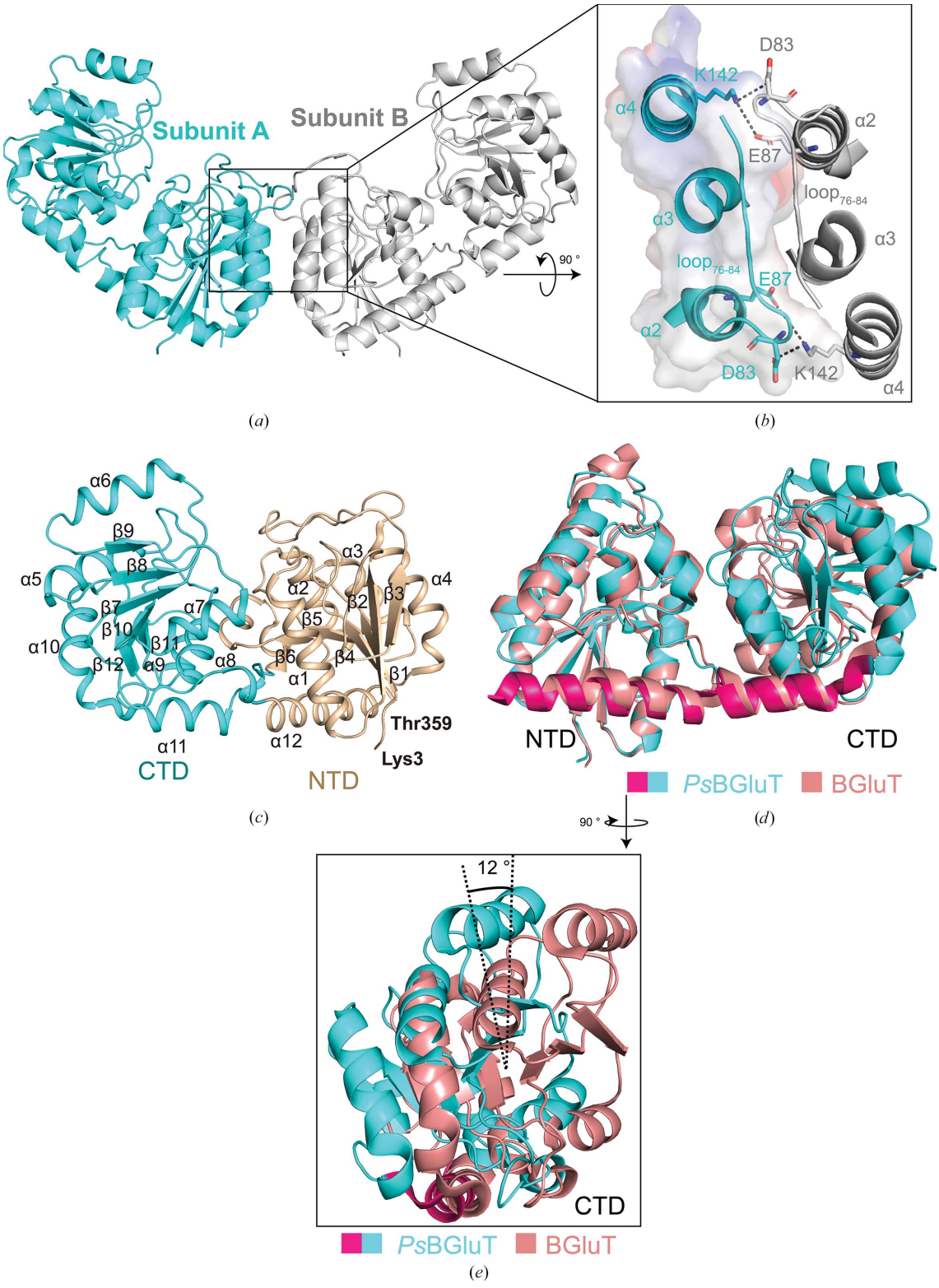

Figure 2
Crystal structure of *Ps*BGluT. (*a*, *b*) The dimeric structure of *Ps*BGluT. The two subunits are colored cyan and gray. The helical bundle at the dimer interface is enlarged as an inset in (*b*). The residues involved in polar interactions at the interface are shown as sticks, with salt bridges indicated by black dashed lines. The three α-helices at the dimeric interface from one subunit of *Ps*BGluT are shown as an electrostatic potential surface. (*c*) Cartoon representation of one *Ps*BGluT subunit, with the NTD and CTD colored cyan and orange, respectively. The secondary-structural elements are labeled sequentially. (*d*) Structural alignment of *Ps*BGluT (cyan and pink) and BGluT from *Synechococcus* sp. PCC 7942 (salmon; PDB entry 5ze7) after superimposing the NTDs of the structures. The C-terminal α-helix of *Ps*BGluT that differs from that of BGluT is colored pink. (*e*) Rotational view of (*d*) showing the angle between the CTDs of *Ps*BGluT and BGluT, where the NTDs from *Ps*BGluT and BGluT in (*d*) are hidden. The rotational angle between the two CTDs as calculated by *angle_between_domains* (https://pymolwiki.org/index.php/Angle_between_domains) is labeled.

NTDs in the apo *Ps*BGluT and *Ps*BGluT–UDP structures, we observed a 15.6° rotation of the two CTDs (Fig. 3*c*). This indicated that UDP binding to the interdomain cleft makes the NTD and CTD domains shift towards each other, consistent with an induced-fit mechanism. This induced-fit effect positions the two domains in proximity, facilitating the glycosyltransfer reaction (Fig. 3*c*). The uracil ring of UDP is fixed by Phe246 through π–π stacking, in addition to a hydrogen bond to Leu247 and Gly245, whereas the O2 and O3 atoms of the ribose moiety of UDP-Glc are stabilized by Glu278 and Asn274 via hydrogen bonds. The pyrophosphate moiety of UDP is fixed by Arg196 and Lys201 from the conserved RX_4K motif via salt bridges, in addition to hydrogen bonds to Gly24, Asn274 and Ala275 (Fig. 3*b*).

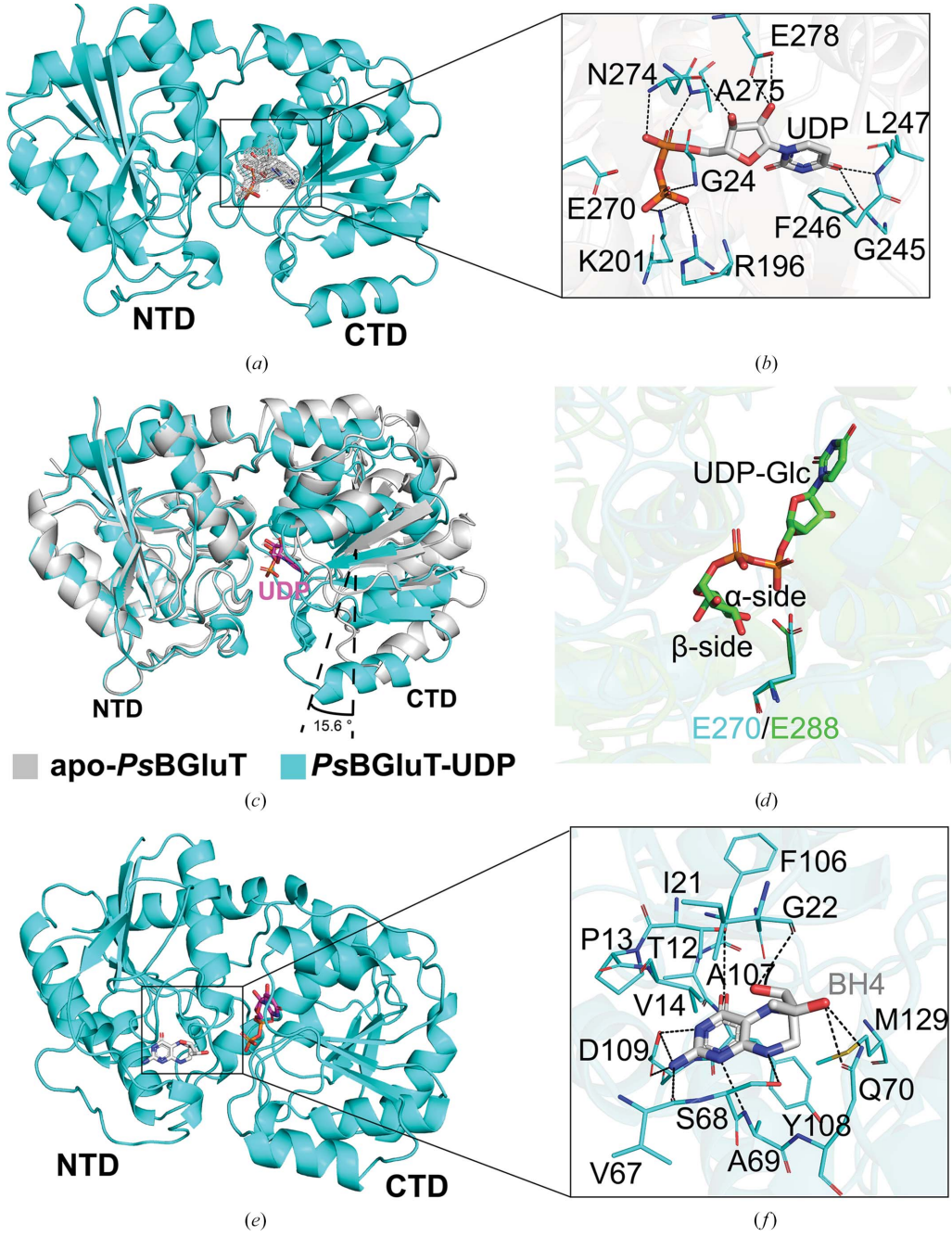

Figure 3
The substrate-binding pocket of *Ps*BGluT. (*a*, *b*) The UDP-binding site. The $2|F_o| - |F_c|$ density map of the UDP molecule contoured at 1.0σ is shown as a mesh. The detailed UDP-binding site is enlarged as an inset. The binding residues and the UDP molecule are shown as sticks. The polar interactions are shown as dashed lines. (*c*) Structural superposition of apo *Ps*BGluT (gray) with *Ps*BGluT–UDP (cyan). The NTDs of the two structures are aligned together to show the relative rotations of the two CTDs, and the rotational angle between the two CTDs as calculated by *angle_between_domains* (https://pymolwiki.org/index.php/Angle_between_domains) is labeled. (*d*) Structural superposition of *Ps*BGluT–UDP (cyan) with Alr3699–UDP-Glc (PDB entry 4xsr; green). The key catalytic residues, Glu270 in *Ps*BGluT and Glu288 in Alr3699, are shown as sticks and labeled. (*e*, *f*) A simulated model of BH_4 binding to *Ps*BGluT. The detailed BH_4-binding site is enlarged as an inset. The binding residues and the BH_4 molecule are shown as sticks. Polar interactions are shown as dashed lines.

Superposition of our *Ps*BGluT–UDP structure on the structure of UDP-Glc-bound Alr3699 (Wang *et al.*, 2016) revealed the putative binding site for the glucose moiety (Fig. 3*d*). It showed that Glu270, which corresponds to Glu288 in Alr3699, interacts with the C3 OH of the glucose moiety via hydrogen bonds. Previous studies proposed that this conserved glutamate in GT-B glycosyltransferases promotes nucleophilic attack on the glucose moiety and charge redistribution for glycosidic bond cleavage. Mutation of this glutamate residue in GT-B glycosyltransferases completely abolishes their enzymatic activity (Wang *et al.*, 2016; Li *et al.*, 2020; Huang *et al.*, 2024), further suggesting that Glu270 in *Ps*BGluT might play an essential role in catalysis. Sequence analysis suggested that these UDP-Glc-binding residues, including Arg196, Lys201, Phe246, Glu270, Asn274 and Glu278, are highly conserved in pterin glycosyltransferases (Supplementary Fig. S1).

To further elucidate the binding mode of the acceptor BH_4, we docked BH_4 into the catalytic pocket at the NTD of *Ps*BGluT (Fig. 3*e*). In the docking model, C2 NH_2 and N3 of BH_4 form salt bridges with Asp108, whereas O4, C6 2′-OH and N8 of BH_4 form hydrogen bonds to Thr12, Gln70 and Ser68, respectively. Furthermore, BH_4 establishes hydrogen bonds and hydrophobic interactions with Thr12–Val14, Ile21–Gly22, Val67–Ala69 from loop L1, Phe106–Tyr108 and Met129 of the NTD (Fig. 3*f*). Notably, the BH_4-binding pocket is rich in hydrophobic residues, which could accommodate the hydrophobic pterin ring (Supplementary Fig. S6). The residues Thr12 and Asp109 of *Ps*BGluT required for BH_4 binding are highly conserved among pterin GTs (Supplementary Fig. S1; Lee *et al.*, 2010), of which Asp109 is proposed to neutralize the positive charges of the BH_4 ring (Supplementary Fig. S7*a*), possessing similar functions to the counterpart residues from *E. coli* 6-carboxytetrahydropterin synthase (Supplementary Fig. S7*b*; Seo *et al.*, 2014), *Staphylococcus aureus* molybdopterin synthase (Supplementary Fig. S7*c*; Daniels *et al.*, 2008) and the human folate receptor (Supplementary Fig. S7*d*; Wibowo *et al.*, 2013).

3.5. The active-site pocket of *Ps*BGluT

GT-B glycosyltransferases are classified into inverting and retaining enzymes. The major difference between these two classes originates from the two loops located at the active-site

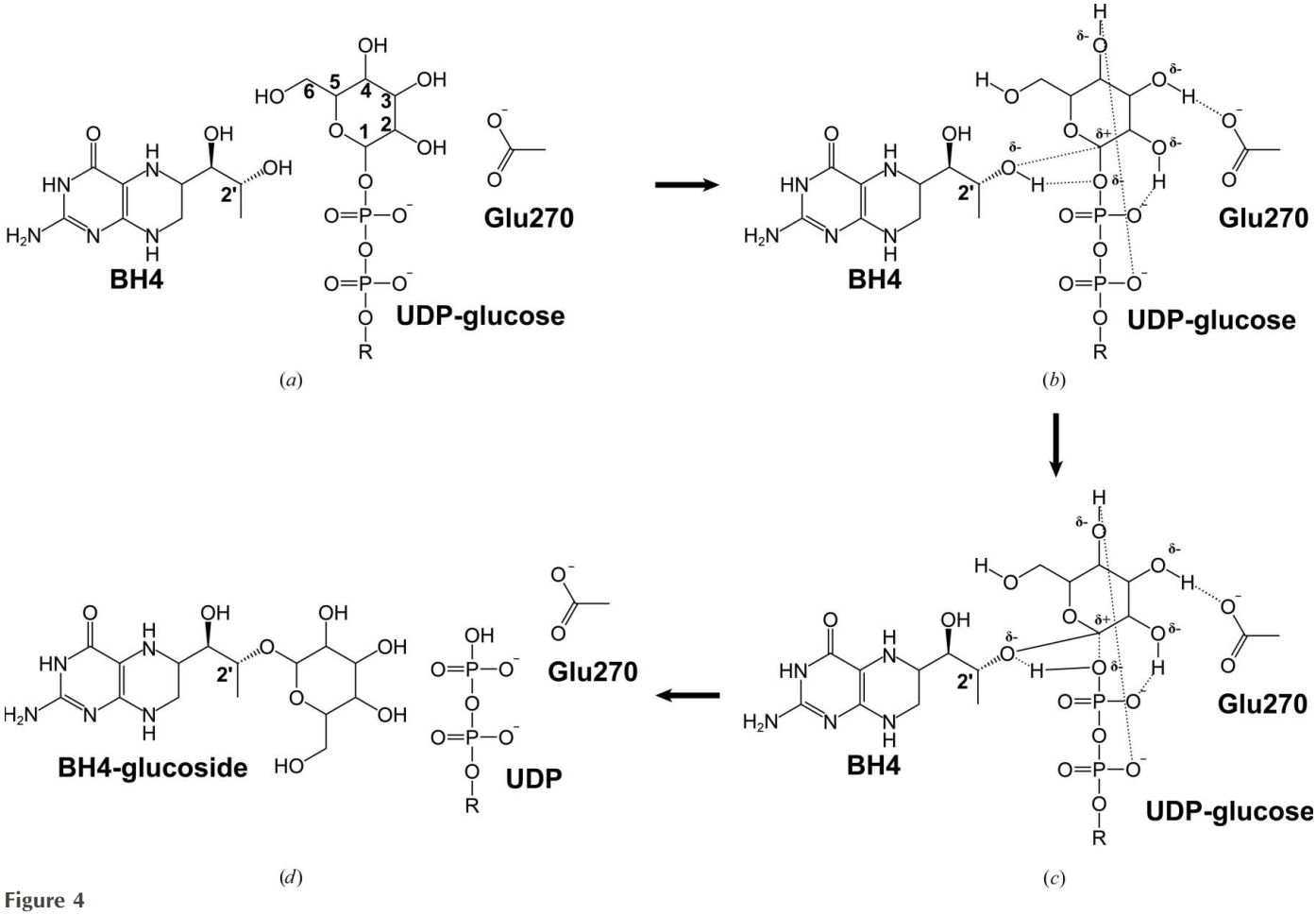

Figure 4
A proposed catalytic mechanism for *Ps*BGluT. (*a*) The substrates UDP-Glc and BH_4 bind to the active-site pocket of *Ps*BGluT. The C atoms of the glucose moiety are numbered sequentially. (*b*) The glucose moiety forms hydrogen bonds to phosphate groups, Glu270 and BH_4, weakening the covalent bond between UDP and glucose. (*c*) During the catalysis, glucose C1 forms a covalent bond with C6 2′-OH of BH_4. (*d*) The products UDP and BH_4-glucoside are synthesized and released from the active-site pocket. The temporary hydrogen bonds are shown as dashed lines.

pocket that bind to the sugar donor and receptor, respectively (Wang *et al.*, 2016; Li *et al.*, 2020; Huang *et al.*, 2024). In the retaining GT WaaG (PDB entry 2iw1), a long loop connecting α11 and β11 stabilizes the pyrophosphate and sugar moieties of the donor in the active-site cleft, whereas the other long loop connecting α1 and β1 binds to the sugar acceptor (Supplementary Fig. S8*a*; Martinez-Fleites *et al.*, 2006). In addition, a conserved glutamate residue (Glu281 in WaaG) is located on the α side of the glucose ring which is required for nucleophilic attack on the glucose moiety (Fig. 3*c*, Supplementary Fig. S8*b*). In contrast, the two corresponding loops in inverting GTs such as VvGT1 (PDB entry 2c1z; Offen *et al.*, 2006) are relatively shorter (Supplementary Fig. S8*c*), and an acidic residue Asp374 is observed on the β side of the glucose ring (Supplementary Fig. S8*d*). *Ps*BGluT possesses two long loops similar to those found in WaaG, in addition to a conserved Glu270 corresponding to Glu281 in WaaG (Fig. 3*c*, Supplementary Figs. S8*a* and S8*b*). These findings strongly indicate that *Ps*BGluT functions as a retaining GT.

Structural analysis, together with previous findings, suggests that *Ps*BGluT employs an S_Ni catalytic mechanism (Li *et al.*, 2020; Wang *et al.*, 2016; Guerin, 2023; Fig. 4). The reaction begins with the binding of UDP-Glc and the acceptor BH_4 in the active site. Hydrogen bonds form between the glucose moiety and the conserved Glu270, as well as between glucose and the nucleophilic C6 2′-OH of BH_4 (Fig. 4*a*). These interactions induce charge redistribution in the pyranose ring, weakening the covalent bond between glucose and UDP and therefore facilitating the formation of a transient oxocarbenium ion at the glucose C1 position. The oxocarbenium ion aligns with UDP and the C6 2′-OH of BH_4 to form a catalytic triad (Fig. 4*b*). Owing to the weak hydrogen-bond interactions between Glu270 and glucose 6-OH, proton dissociation occurs rapidly, further destabilizing the pyranose ring and favoring nucleophilic attack by BH_4. This leads to BH_4–glucose covalent-bond formation (Fig. 4*c*). The final products, BH_4-glucoside and UDP, are then released from the catalytic pocket to accomplish the catalytic cycle (Fig. 4*d*).

4. Summary

We have reported structures of apo *Ps*BGluT and UDP-bound *Ps*BGluT in this study, which enabled us to elucidate the substrate-binding mode of *Ps*BGluT and its catalytic mechanism. Structural analysis revealed distinct features at the active-site pocket of *Ps*BGluT, which differs from other retaining GT-B glycosyltransferases. This study not only advances our knowledge of the structure and catalytic mode of GT-B glycosyltransferases, but also provides a further basis for investigating the mechanisms of the photosynthetic signaling pathway in cyanobacteria. However, whether *Ps*BGluT binds to other sugar donors or sugar acceptors requires further exploration.

Acknowledgements

The authors thank Professor ZhongLiang Zhu from the Core Facility Center for Life Sciences at the University of Science and Technology of China for support with X-ray crystal data collection and Dr Jie Zhu for isolation of *Pseudanabaena* sp. Chao 1811. We greatly appreciate the significant efforts of the three referees, especially referee 3, for reviewing our article extremely carefully and for giving us useful advice.

Conflict of interest

The authors declare no conflicts of interest.

Data availability

The crystallographic data for apo *Ps*BGluT and the *Ps*BGluT–UDP complex have been deposited in the Protein Data Bank with accession codes 9v0w and 9v0l, respectively.

Funding information

This work was funded by the National Natural Science Foundation of China (Grant No. 32430001) and Chaohu Lake Biological Resource Investigation and Research Project (Grant No. 2020-340181-77-01-037328).

References

Agirre, J., Atanasova, M., Bagdonas, H., Ballard, C. B., Baslé, A., Beilsten-Edmands, J., Borges, R. J., Brown, D. G., Burgos-Mármol, J. J., Berrisford, J. M., Bond, P. S., Caballero, I., Catapano, L., Chojnowski, G., Cook, A. G., Cowtan, K. D., Croll, T. I., Debreczeni, J. É., Devenish, N. E., Dodson, E. J., Drevon, T. R., Emsley, P., Evans, G., Evans, P. R., Fando, M., Foadi, J., Fuentes-Montero, L., Garman, E. F., Gerstel, M., Gildea, R. J., Hatti, K., Hekkelman, M. L., Heuser, P., Hoh, S. W., Hough, M. A., Jenkins, H. T., Jiménez, E., Joosten, R. P., Keegan, R. M., Keep, N., Krissinel, E. B., Kolenko, P., Kovalevskiy, O., Lamzin, V. S., Lawson, D. M., Lebedev, A. A., Leslie, A. G. W., Lohkamp, B., Long, F., Malý, M., McCoy, A. J., McNicholas, S. J., Medina, A., Millán, C., Murray, J. W., Murshudov, G. N., Nicholls, R. A., Noble, M. E. M., Oeffner, R., Pannu, N. S., Parkhurst, J. M., Pearce, N., Pereira, J., Perrakis, A., Powell, H. R., Read, R. J., Rigden, D. J., Rochira, W., Sammito, M., Sánchez Rodríguez, F., Sheldrick, G. M., Shelley, K. L., Simkovic, F., Simpkin, A. J., Skubak, P., Sobolev, E., Steiner, R. A., Stevenson, K., Tews, I., Thomas, J. M. H., Thorn, A., Valls, J. T., Uski, V., Usón, I., Vagin, A., Velankar, S., Vollmar, M., Walden, H., Waterman, D., Wilson, K. S., Winn, M. D., Winter, G., Wojdyr, M. & Yamashita, K. (2023). *Acta Cryst.* D**79**, 449–461.

Alexander, J. A. N. & Locher, K. P. (2023). *Curr. Opin. Struct. Biol.* **79**, 102547.

Casañal, A., Lohkamp, B. & Emsley, P. (2020). *Protein Sci.* **29**, 1055–1064.

Choi, Y. K., Hwang, Y. K. & Park, Y. S. (2001). *FEBS Lett.* **502**, 73–78.

Daniels, J. N., Wuebbens, M. M., Rajagopalan, K. V. & Schindelin, H. (2008). *Biochemistry*, **47**, 615–626.

Evans, P. R. & Murshudov, G. N. (2013). *Acta Cryst.* D**69**, 1204–1214.

Guerin, M. E. (2023). *J. Biol. Chem.* **299**, 105006.

Holm, L., Laiho, A., Törönen, P. & Salgado, M. (2023). *Protein Sci.* **32**, e4519.

Huang, W., Song, J., Sun, T., He, Y., Li, X., Deng, Z. & Long, F. (2024). *Nat. Commun.* **15**, 1659.

Iyer, S. R., Tidemand, K. D., Babicz, J. T. Jr, Jacobs, A. B., Gee, L. B., Haahr, L. T., Yoda, Y., Kurokuzu, M., Kitao, S., Saito, M., Seto, M., Christensen, H. E. M., Peters, G. H. J. & Solomon, E. I. (2021). *Proc. Natl Acad. Sci. USA*, **118**, e2022379118.

Jumper, J., Evans, R., Pritzel, A., Green, T., Figurnov, M., Ronneberger, O., Tunyasuvunakool, K., Bates, R., Žídek, A., Potapenko, A., Bridgland, A., Meyer, C., Kohl, S. A. A., Ballard, A. J., Cowie, A., Romera-Paredes, B., Nikolov, S., Jain, R., Adler, J., Back, T.,

Petersen, S., Reiman, D., Clancy, E., Zielinski, M., Steinegger, M., Pacholska, M., Berghammer, T., Bodenstein, S., Silver, D., Vinyals, O., Senior, A. W., Kavukcuoglu, K., Kohli, P. & Hassabis, D. (2021). *Nature*, **596**, 583–589.
Khaled, G., Benvegnu, T., Amin, K., Tranchimand, S. & Chamieh, H. (2025). *Anal. Biochem.* **702**, 115826.
Kovalevskiy, O., Nicholls, R. A., Long, F., Carlon, A. & Murshudov, G. N. (2018). *Acta Cryst.* D**74**, 215–227.
Lairson, L. L., Henrissat, B., Davies, G. J. & Withers, S. G. (2008). *Annu. Rev. Biochem.* **77**, 521–555.
Lee, Y. G., Kim, A. H., Park, M. B., Kim, H.-L., Lee, K. H. & Park, Y. S. (2010). *Appl. Environ. Microbiol.* **76**, 7658–7661.
Li, Q., Li, C., Zhong, J., Wang, Y., Yang, Q., Wang, B., He, W., Huang, J., Lin, S. & Qi, F. (2025). *Metab. Eng.* **87**, 49–59.
Li, Y., Yao, Y., Yang, G., Tang, J., Ayala, G. J., Li, X., Zhang, W., Han, Q., Yang, T., Wang, H., Mayo, K. H. & Su, J. (2020). *Front. Microbiol.* **11**, 1050.
Martinez-Fleites, C., Proctor, M., Roberts, S., Bolam, D. N., Gilbert, H. J. & Davies, G. J. (2006). *Chem. Biol.* **13**, 1143–1152.
Morris, G. M., Huey, R., Lindstrom, W., Sanner, M. F., Belew, R. K., Goodsell, D. S. & Olson, A. J. (2009). *J. Comput. Chem.* **30**, 2785–2791.
Mu, W., Hu, N., Zhang, L.-H., Jiang, W., Yan, T., Zhang, T., Liu, A., Zhang, Y.-Q., Zhao, J., Shi, L. & Liu, L.-N. (2022). *Phytomedicine*, **102**, 154146.
Noguchi, Y., Ishii, A., Matsushima, A., Haishi, D., Yasumuro, K., Moriguchi, T., Wada, T., Kodera, Y., Hiroto, M., Nishimura, H., Sekine, M. & Inada, Y. (1999). *Mar. Biotechnol.* **1**, 207–210.
Offen, W., Martinez-Fleites, C., Yang, M., Kiat-Lim, E., Davis, B. G., Tarling, C. A., Ford, C. M., Bowles, D. J. & Davies, G. J. (2006). *EMBO J.* **25**, 1396–1405.
Poon, B. K., Terwilliger, T. C. & Adams, P. D. (2024). *Protein Sci.* **33**, e4992.
Seo, K. H., Zhuang, N., Park, Y. S., Park, K. H. & Lee, K. H. (2014). *Acta Cryst.* D**70**, 1212–1223.
Shyam, R., Sekhar Panda, H., Mishra, J., Jyoti Panda, J. & Kour, A. (2024). *Clin. Chim. Acta*, **559**, 119725.
Singh, V. K., Jha, S., Rana, P., Mishra, S., Kumari, N., Singh, S. C., Anand, S., Upadhye, V. & Sinha, R. P. (2023). *Int. J. Mol. Sci.* **24**, 12381.
Vagin, A. & Teplyakov, A. (2010). *Acta Cryst.* D**66**, 22–25.
Wang, X.-P., Jiang, Y.-L., Dai, Y.-N., Cheng, W., Chen, Y. & Zhou, C.-Z. (2016). *Glycobiology*, **26**, 520–531.
Wibowo, A. S., Singh, M., Reeder, K. M., Carter, J. J., Kovach, A. R., Meng, W., Ratnam, M., Zhang, F. & Dann, C. E. (2013). *Proc. Natl Acad. Sci. USA*, **110**, 15180–15188.
Zheng, Y., Anderson, S., Zhang, Y. & Garavito, R. M. (2011). *J. Biol. Chem.* **286**, 36108–36118.
Zhu, J., Yang, F., Du, K., Wei, Z.-L., Wu, Q.-F., Chen, Y., Li, W.-F., Li, Q. & Zhou, C.-Z. (2023). *Environ. Microbiome*, **18**, 3.

STRUCTURAL BIOLOGY
COMMUNICATIONS

Volume 81 (2025)

Supporting information for article:

Structural analysis of the tetrahydrobiopterin glucosyltransferase *Ps*BGluT from *Pseudanabaena* sp. Chao 1811

Ruijie Zang, Yongliang Jiang and Cong-Zhao Zhou

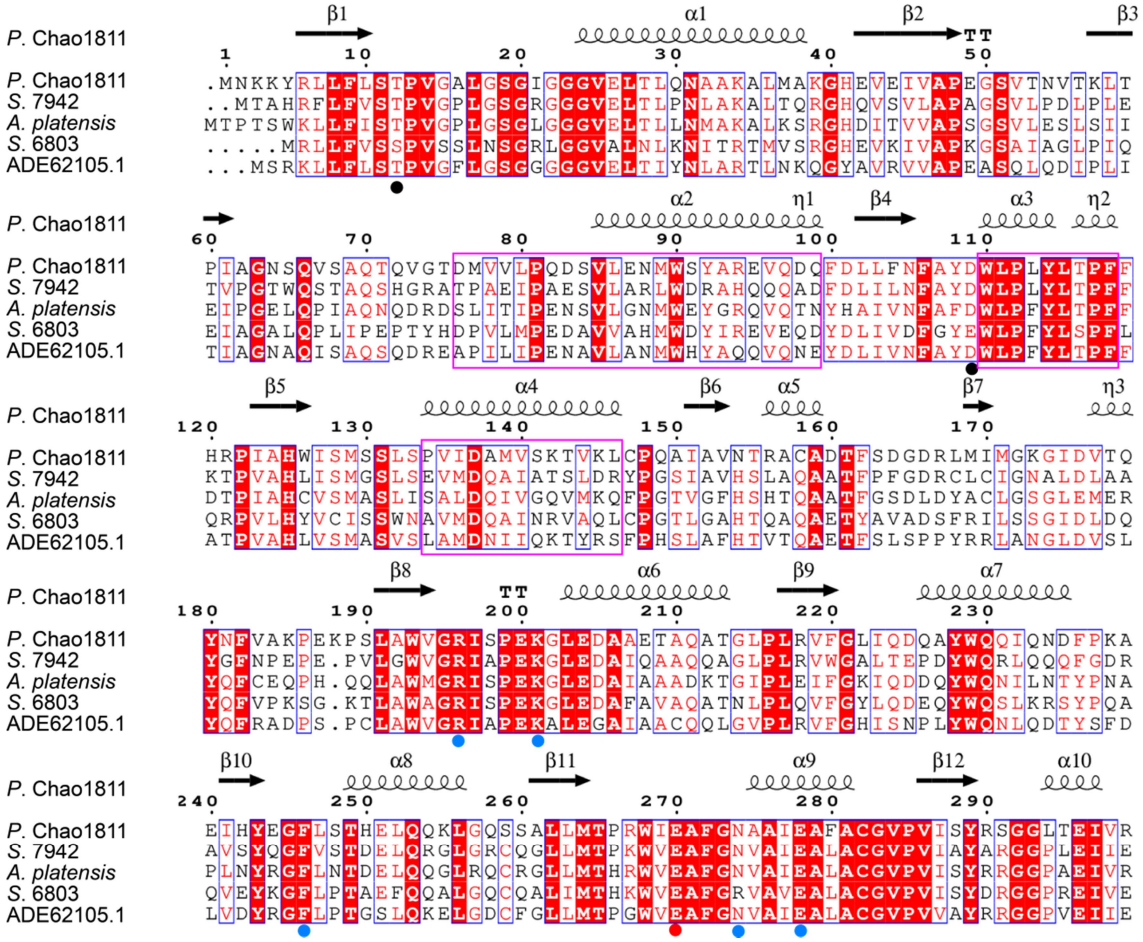

Figure S1 Multiple sequence alignment of *Ps*BGluT and its homologs. *P*. Chao 1811: *Pseudanabaena* sp.Chao 1811; *S*. 7942: *Synechococcus elongatus* PCC.7942; *A. platensis*: *Arthrospira platensis*; *S*. 6803: *Synechocystis* PCC. 6803; ADE62105.1 : a putative cyanobacterial pterin glycosyltransferase. The putative BH4-binding residues are highlighted with black circles, whereas the residues for UDP-glucose binding are marked by blue circles. The key glutamate residue required for the catalysis is labeled by a red circle. The residues involved in formation of dimeric interface are shown in magenta rectangles.

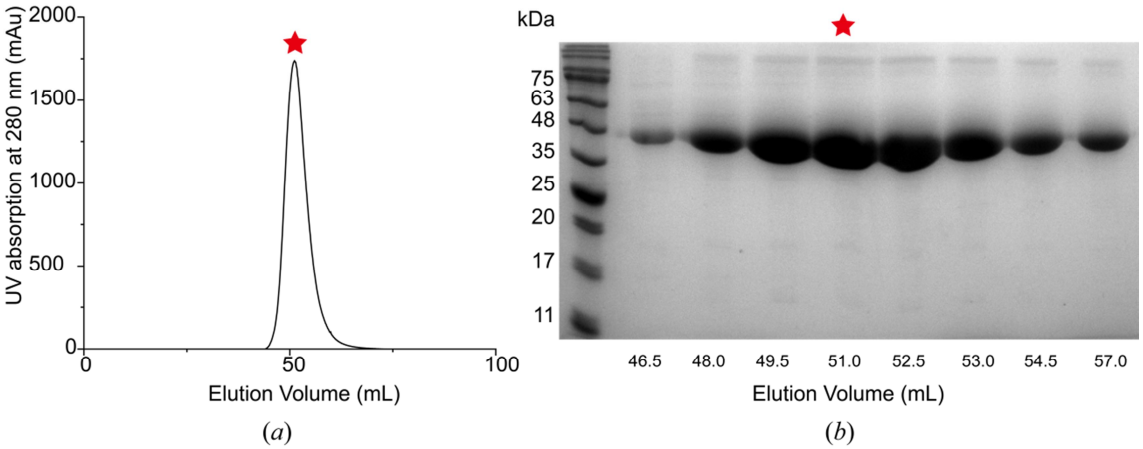

Figure S2 Purification of *Ps*BGluT. (*a*) Gel-filtration chromatography profile of *Ps*BGluT. The elution peak is about 52 mL, which is highlighted with a red star.(*b*) Sodium dodecyl sulfate polyacrylamide gel electrophoresis (SDS-PAGE) analysis of *Ps*BGluT protein which is from the elution peak in (*a*). The elution volume for the protein in each lane of the SDS-PAGE is labeled.

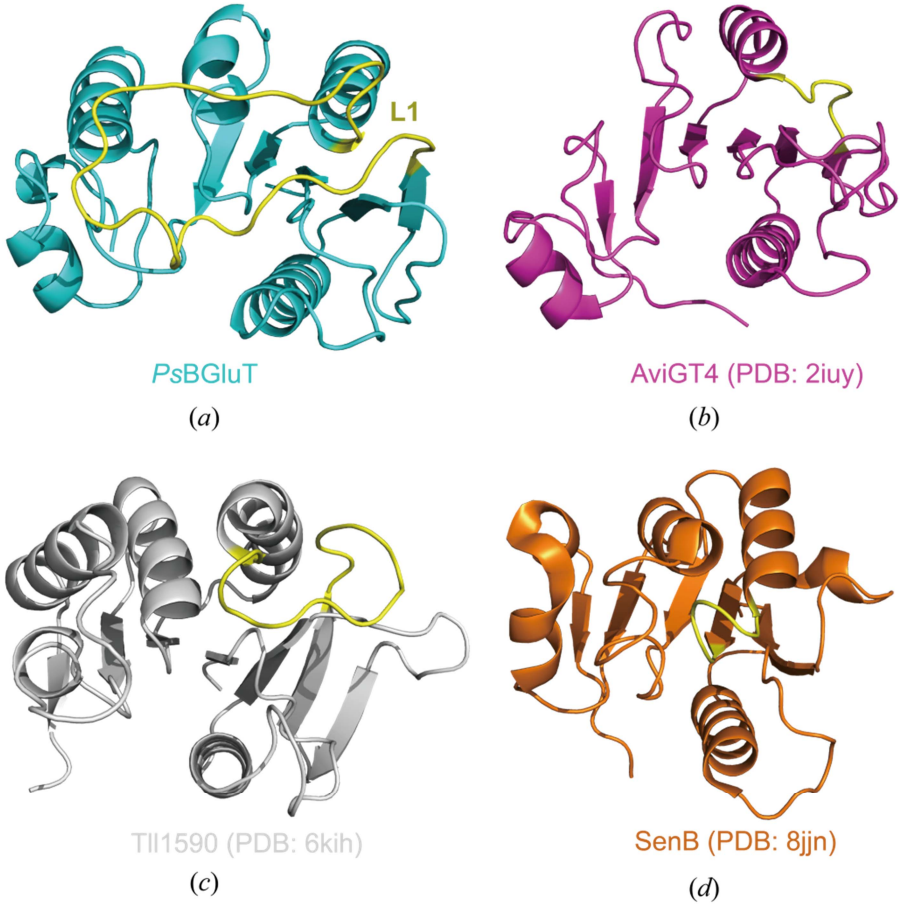

Figure S3 Structural comparisons of *Ps*BGluT NTDs and its homologs. The L1 loop of *Ps*BGluT at active-site pocket, and the counterpart loops in other homologs, are colored yellow. (*a*) Apo-*Ps*BGluT from *Pseudanabaena* sp. Chao 1811. (*b*) AviGT4 from *Streptomyces viridochromogenes* (PDB: 2iuy). (c) Tll1590 from *Thermosynechococcus vestitus* (PDB: 6kih). (d) SenB from *Variovorax paradoxus* (PDB: 8jjn).

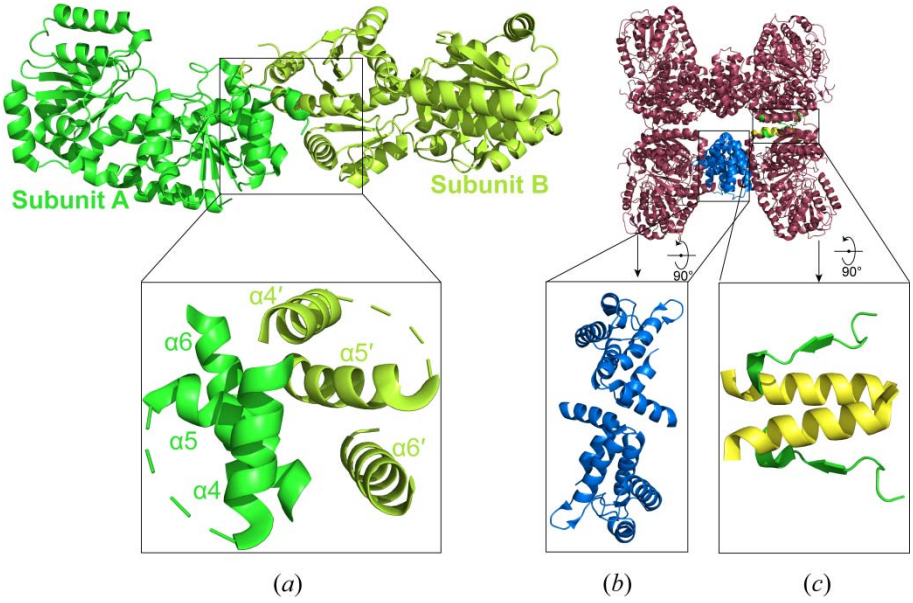

Figure S4 The oligomeric interfaces of different GT-B glycosyltransferases. (*a*) The structure of Alr3699 dimer from *Anabaena* sp. PCC 7120 (PDB: 4xso), with the dimer interface zoomed-in as an inset. (*b*, *c*) The structure of AtSUS tetramer from *Arabidopsis thaliana* (PDB: 3s27), with the two different interfaces zoomed-in as insets.

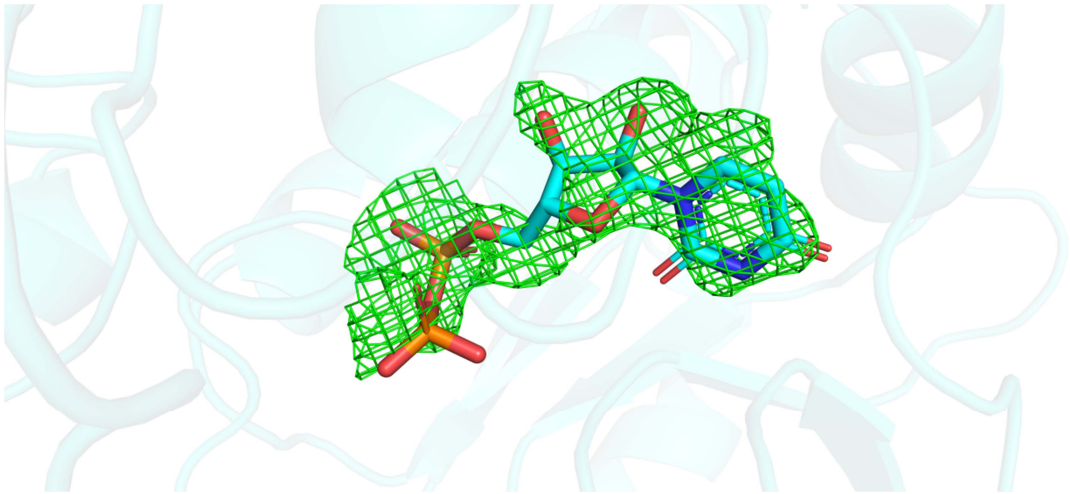

Figure S5 The omit-map of UDP molecule contoured at 2.5 δ in the structure of *Ps*BGluT-UDP is shown in green.

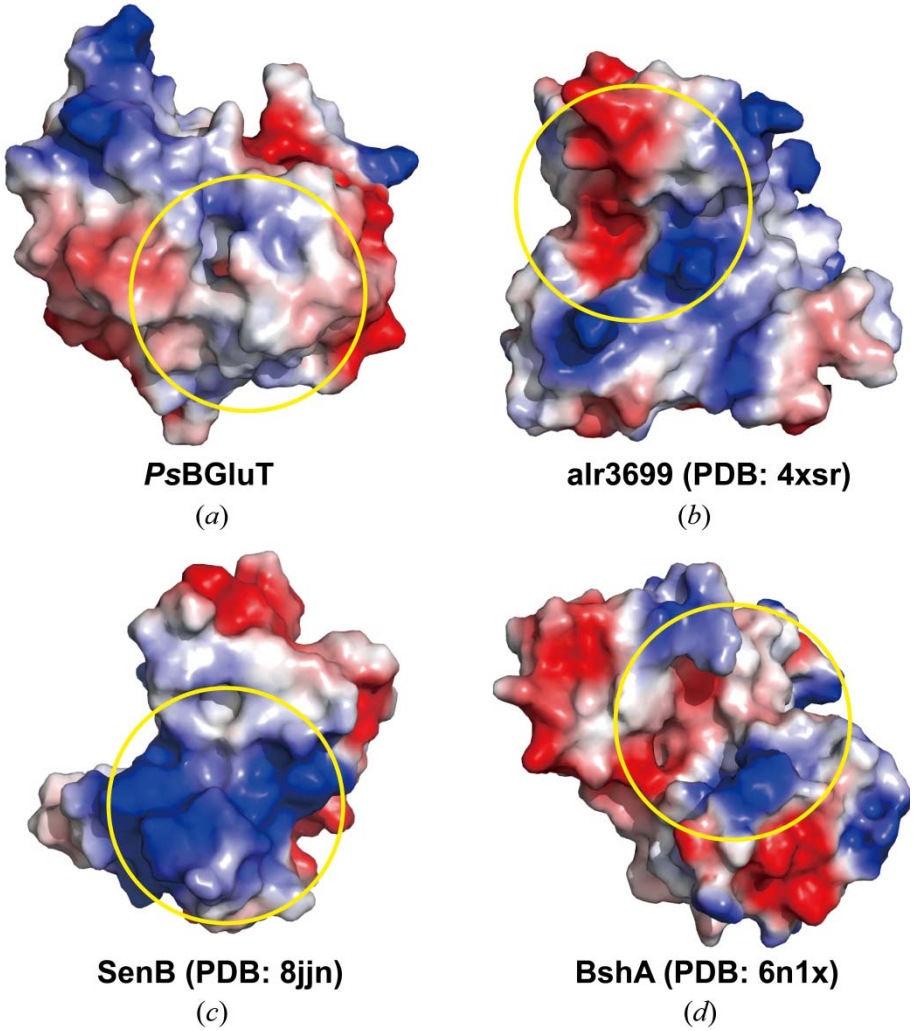

Figure S6 The electrostatic surface properties of the NTDs of different GT-B glycosyltransferases. (*a*) *Ps*BGluT from *Pseudanabaena* spp. Chao 1811. (*b*) Alr3699 from *Anabaena* sp. PCC 7120 (PDB: 4xsu). (*c*) SenB from *Variovorax paradoxus* (PDB: 8jjn). (*d*) BshA from *Staphylococcus aureus* (PDB: 6n1x). The substrate-binding pocket is indicated by a yellow circle.

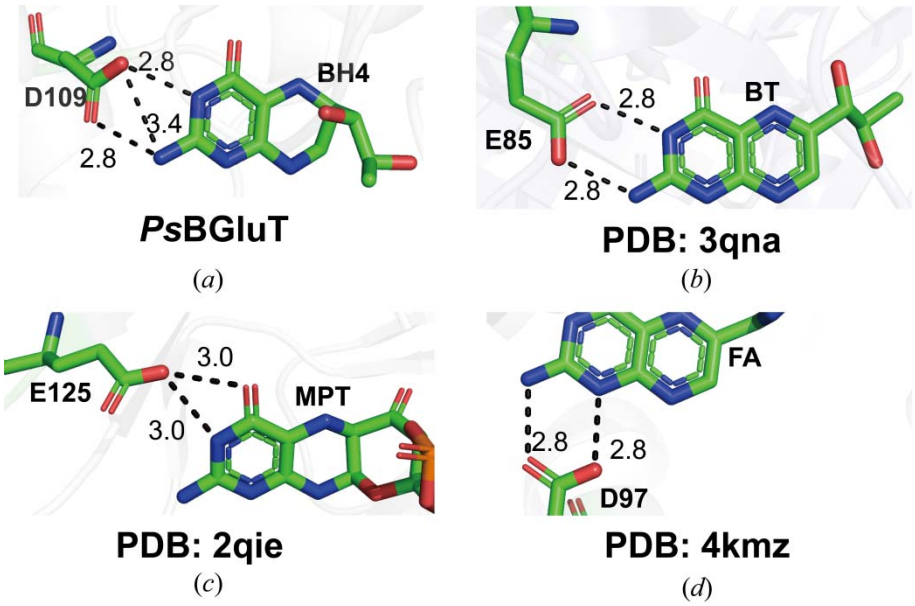

Figure S7 Comparison of the pterin-like binding site in different proteins. The key acidic residue required for binding to the substrate is shown as sticks. The hydrogen bonds or salt bridges are depicted as black dashes, and their lengths (Å) are labeled. (*a*) *Ps*BGluT from *Pseudanabeana* sp. Chao 1811. (*b*) 6-carboxytetrahydropterin synthase from *Escherichia coli* (PDB: 3qna). (*c*) Molybdopterin synthase from *Staphylococcus aureus* (PDB: 2qie). (*d*) Folate receptor from *Homo sapians* (PDB: 4kmz). BH4, tetrahydrobiopterin; BT, biopterin; MPT, molybdopterin; FA, folate.

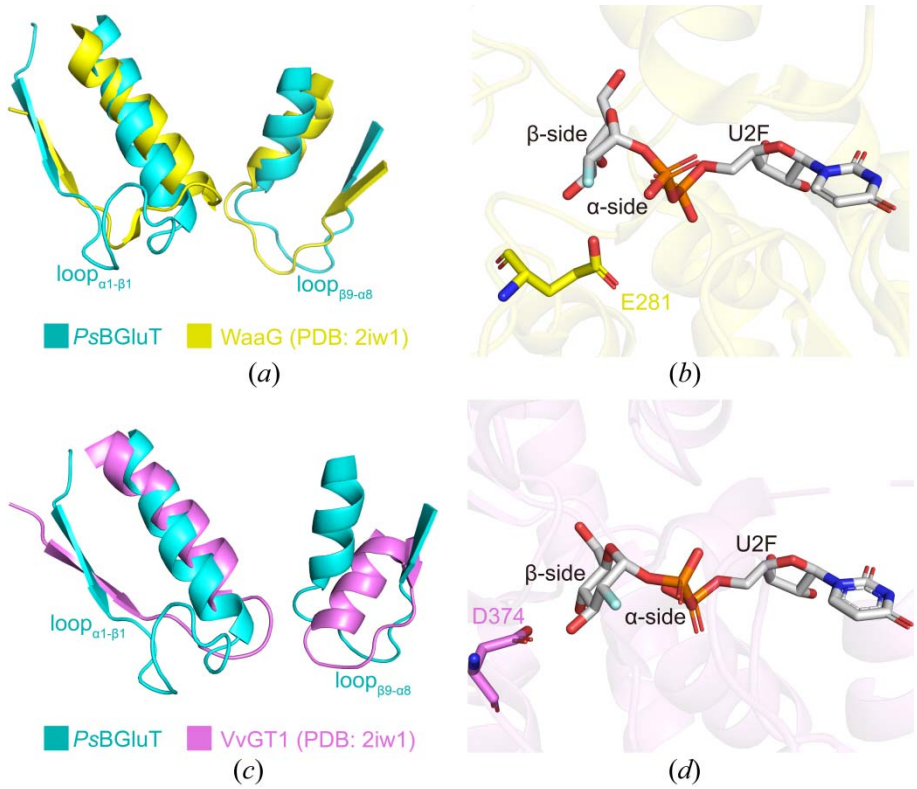

Figure S8 Structural comparisons of the retaining and inverting GTs. (*a*) Comparison of *Ps*BGluT (cyan) against the retaining GT WaaG (PDB: 2iw1, yellow). The RMSD between them is 2.955 (over 35 C_α atoms). (*b*) A zoomed-in view of the catalytic center of WaaG (PDB: 2iw1). (*c*) Comparison of *Ps*BGluT against the inverting GT VvGT1 (PDB: 2c1x, violet). The RMSD between them is 1.891 (over 16 C_α atoms). (*d*) A zoomed-in view of the catalytic center of VvGT1 (PDB: 2c1x). The structures of *Ps*BGluT, WaaG and VvGT1 are colored in cyan, yellow and violet, respectively. U2F, uridine-5′-diphosphate-2-deoxy-2-fluoro-α-D-glucose.